

Prevailing Triaxial Shapes in Heavy Nuclei Driven by π Meson

T. Otsuka,^{1,2,3,4,*} Y. Tsunoda,^{5,6} Y. Utsuno,^{3,5} N. Shimizu,^{5,6} T. Abe,² and H. Ueno²

¹*Department of Physics, The University of Tokyo, 7-3-1 Hongo, Bunkyo, Tokyo 113-0033, Japan*

²*RIKEN Nishina Center, 2-1 Hirosawa, Wako, Saitama 351-0198, Japan*

³*Advanced Science Research Center, Japan Atomic Energy Agency, Tokai, Ibaraki 319-1195, Japan*

⁴*KU Leuven, Instituut voor Kern- en Stralingsfysica, 3000 Leuven, Belgium*

⁵*Center for Nuclear Study, The University of Tokyo, 7-3-1 Hongo, Bunkyo, Tokyo 113-0033, Japan*

⁶*Center for Computational Sciences, University of Tsukuba, 1-1-1 Tennodai, Tsukuba, Ibaraki, 305-8577, Japan*
(Dated: March 21, 2023)

Virtually any object can rotate: the rotation of a rod or a linear molecule appears evident, but a number of objects, including a simple example of H_2O molecule, are of complex shapes and rotate in complicated manners. While the rotation provides various intriguing physics cases, the primary picture for atomic nuclei was simple. Rotational bands have been observed for many nuclei, and their basic picture is considered to have been established in 1950's. We, however, show that this traditional picture is superseded with a novel picture arising from basic characteristics of the nuclear forces. In the traditional view, as stressed by Aage Bohr in his Nobel lecture, most of heavy nuclei are like axially-symmetric prolate ellipsoids (i.e., with two shorter axes of equal length), rotating about one of the short axes, like a rod. In the present picture, however, in many cases, the lengths of these three axes are all different, called triaxial. The triaxial shape yields more complex rotations, which actually reproduce experimental data as shown by state-of-the-art Configuration Interaction calculations, on supercomputers. The key to differentiate the two pictures is the nuclear tensor force, which is known to produce the shell evolution in exotic nuclei, a major agenda of Rare-Isotope physics. We now demonstrate that the same tensor force generates, in many nuclei, the triaxiality, fading the prolate-ellipsoid dominance away. The tensor force is a direct consequence of one π meson exchange between nucleons, and the present finding is regarded as the first explicit or visible case that elementary particles directly affect nuclear shapes. The importance of the explicit tensor force is in the same line as Weinberg's modeling of nuclear forces. This feature makes the new picture robust, and may cast challenges for other many-body systems having spin-dependent forces. Substantial impacts on superheavy nuclei and fission are anticipated. This study sheds lights on the earlier suggestion of dominant triaxiality by Davydov, a Ukrainian physicist.

I. INTRODUCTION REFERRING TO MOLECULAR ROTATION

The atomic nucleus comprises Z protons and N neutrons, which are collectively called nucleons. With the mass number $A=Z+N$, a given nucleus is labelled as AX where X denotes the element, e.g., ^{166}Er for erbium-166 ($Z=68$). The nucleus, as an assembly of many nucleons, exhibits a clear surface with a certain shape. In many nuclei, the shape is an ellipsoid, which rotates [1–3]. There has been the conventional text-book picture for nuclear shape and rotation, as stressed by Aage Bohr in his Nobel-prize lecture in 1975 [4]. The present work, however, depicts a different picture based on recent studies that were infeasible in earlier days. Before an in-depth description of the major outcome, we overview the rotation of molecular systems, because it is easier to view. Figures 1a-b schematically display the rotation of diatomic (O_2) and triatomic (H_2O) molecules [5]. The O_2 molecule is like a rod, and rotates about an axis perpendicular to the axis connecting the two O atoms (see Fig. 1a). It cannot rotate about the axis connecting two atoms, because the quantum state does not change by such rotation.

The situation with the H_2O molecule is more complex. As shown in Fig. 1b, this molecule can rotate about more than one axis. Thus, if the molecule has a complex configuration of atoms, its rotational motion occurs about multiple axes.

A nuclear analogy to the O_2 molecule can be found in a nucleus deformed to a prolate ellipsoid (see Fig. 1c), where the ellipsoid is stretched in the vertical axis in the paper plane (side view), with a nuclear quantum state invariant under the rotation about the vertical axis (top view). This invariance is called *axial-symmetry*, and the vertical axis here is called the *symmetry axis*. In quantum mechanics, no rotational motion arises about the symmetry axis because the state does not change, like di-atomic molecule (see Fig. 1a). On the other hand, the ellipsoid can rotate about an axis perpendicular to the symmetry axis (side view).

The axial-symmetry can be broken in reality. The cross section of the ellipsoid then becomes an ellipse as shown in the top view of Fig. 1d. The rotation can now occur about the axis perpendicular to this cross section, as seen in the right drawing of this panel. Although details are different, this is basically similar to the H_2O molecule case: a complex object can rotate in multiple ways.

II. NUCLEAR ELLIPSOIDAL DEFORMATION

Assuming an ellipsoidal deformation of nuclear shape, it is defined concretely with axes R_x, R_y and R_z shown in Fig. 1e, where the standard convention for the axis lengths $R_z \geq R_x \geq R_y$ is taken. The ellipsoid is viewed from two different angles, A and B. The prolate ellipsoid is shown in Fig. 1f where $R_x=R_y$ holds. The ellipsoid without the axial-symmetry is shown in Fig. 1g, where the three axes take different lengths.

* otsuka@phys.s.u-tokyo.ac.jp

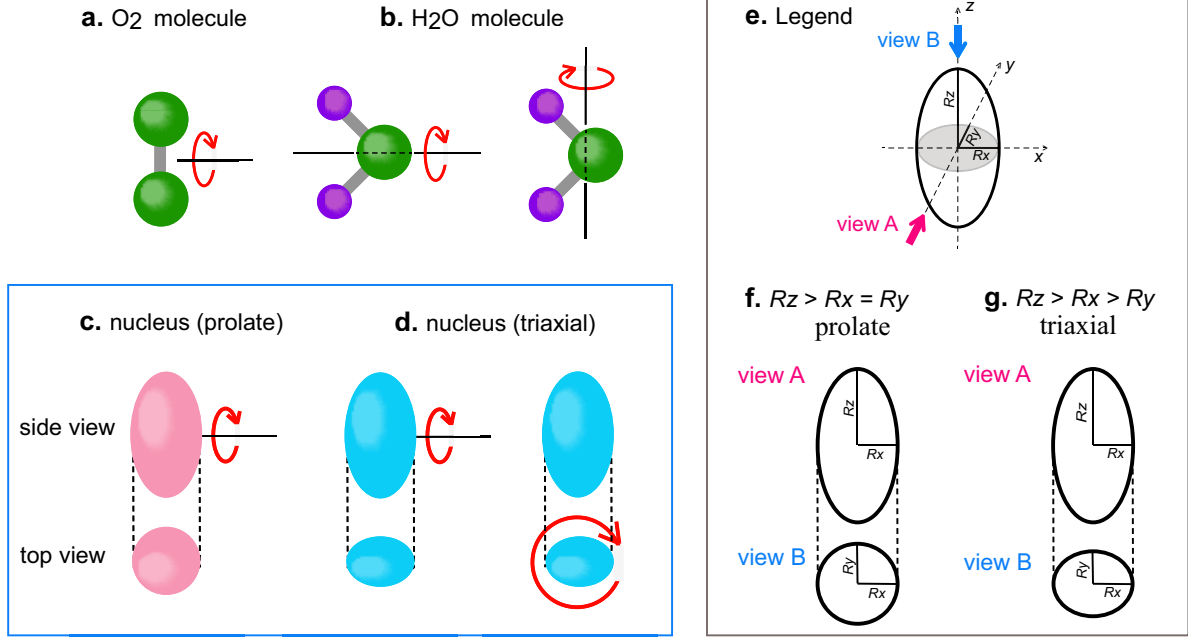


FIG. 1. Schematic illustrations of the rotations of molecules and atomic nuclei. **a** O_2 molecule. **b** H_2O molecule. **c** prolate and **d** triaxial nuclear shapes. **e** Legend. **f**, **g** Principal axes of prolate and triaxial ellipsoids.

This feature is called *triaxial*. The ellipsoid shows quadrupole moments: $Q_0 \propto \langle 2z^2 - x^2 - y^2 \rangle$ and $Q_2 \propto \langle x^2 - y^2 \rangle$, where $\langle \rangle$ implies integral inside the surface with a uniform density. The prolate shape is characterized by positive Q_0 and vanishing Q_2 , whereas the triaxiality by finite Q_2 . We show, in this paper, the unexpected preponderance of the triaxiality, its consequences in nuclear rotation and its robustness rooted in nuclear forces.

The mechanism towards deformed nuclear shapes is schematically depicted in Fig. 2a, where short-range attractive forces between nucleons produce more binding energies for nucleons closely configured (lower object) than for nucleons sparsely spread with longer mutual distances (upper object). The Jahn-Teller effect [7] also contributes to the present formation of the ellipsoidal shape. From now on, the nucleus is treated as a multi-nucleon quantum system, and the quadrupole moments are calculated from their wave functions. The nucleus is then connected to the afore-mentioned ellipsoid with the same quadrupole moments.

The present attraction is much stronger between a proton and a neutron than between two neutrons or between two protons. This implies that the deformation becomes strong if there are sufficiently large numbers of active (or valence) protons and active neutrons, outside the inert core (see Fig. 2a). On the other hand, if the protons (neutrons) form a closed shell, as the closed shell is spherical, the neutrons (protons) also form a spherical shape.

Different nuclear shapes result in visible differences in observables. Figure 2c exhibits the global systematics of the level energies of the lowest state of spin/parity $J^P=2^+$ for even-Z and even-N (*even-even*) nuclei, on top of the $J^P=0^+$

ground state. For doubly-magic nuclei, the excitation from the ground state can be made by moving a nucleon over a magic gap. This requires a large amount of energy, meaning a high excitation energy. There are high spikes in Fig. 2c with the excitation energies more than 2 MeV (see green open circles). These spikes correspond to conventional ($N=8, 20, 28, 50, 82, 126$) or new ($N=16, 32, 34, 40$) magic numbers. Beyond $N \sim 40$, most of the points (blue closed circles) show low excitation energies down to several tens of keV. An example of such low excitation energies is shown for the nucleus, ^{166}Er , in the yellow-shaded part of Fig. 2b, which displays the lowest states of $J^P=2^+, 4^+$ and 6^+ . Next to these experimental levels, the rotational excitation energy, $E_x(J) = \alpha J(J+1)$, is shown with the value of α adjusted to the measured 2^+ level energy, in a remarkable agreement for $J^P=4^+$ and 6^+ . We thus consider that a strongly deformed ellipsoid like the lower part of panel a, rotates with $J^P=2^+, 4^+$ and 6^+ . Similar rotational bands have been observed in many heavy nuclei. The systematics shown in Fig. 2c exhibits many nuclei with the first 2^+ state, denoted as 2^+_1 , at a very low excitation energy. This implies large moments of inertia indicative of strong ellipsoidal deformation.

Figure 2b displays level energies of ^{124}Sn , where the $Z=50$ proton closed shell results in a spherical shape for its ground state. Its $J^P=2^+_1$ level is lying high, partly because of the absence of a mechanism like Fig. 2a. This feature is depicted by closed green circles in Fig. 2c, forming a minor fraction of the points.

The strong ellipsoidal deformation (blue circles in Fig. 2c) is thus an important and dominating trend of heavy nuclei. While Fig. 1c, d display two cases of the shape deformation,

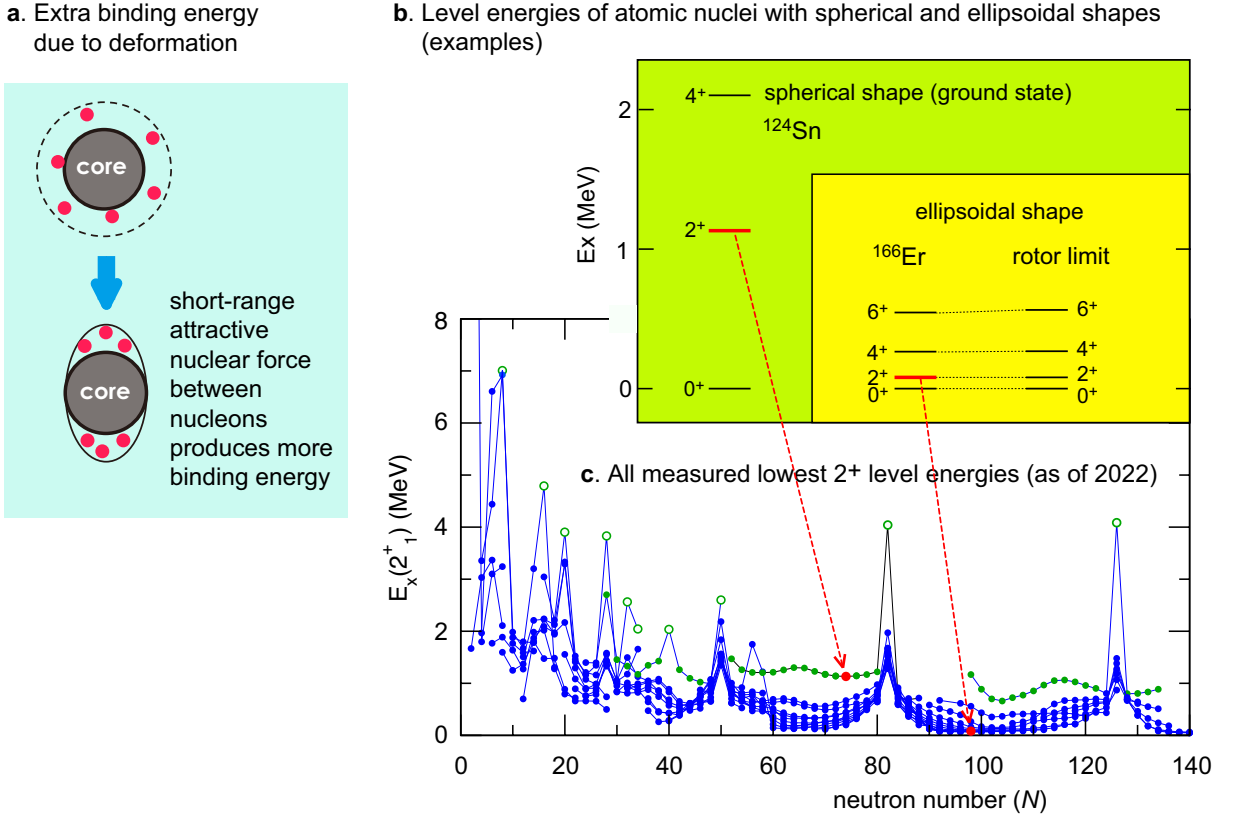


FIG. 2. Overview of the 2^+_1 states. **a** Mechanism to drive ellipsoidal deformation. **b** Examples of spherical and deformed cases with the rotational level energies. **c** All measured lowest 2^+ level energies of even-even nuclei as of the year 2022, based on the data taken from NuDat 3.0 [6].

the axially symmetric shape (panel c) has been considered to occur in most cases, since Bohr and Mottelson argued [1, 4]. This picture has been a textbook item over 70 years [8–10], and many works were made on top of it, for instance, the fission mechanism [11, 12]. We sketch this traditional picture first.

The surface tension of a liquid drop generally makes its shape spherical. The nuclear shape was considered to be an equilibrium between this tension and the force causing the deformation *à la* Fig. 2a. An axially-symmetric ellipsoid is then favored over a triaxial one, because of the constant curvature in the xy plane (see Fig. 1f). The rotation of the rigid body is described, for instance, in textbooks [8, 9]. As a many-nucleon problem, Kumar and Baranger [13] performed the “pairing-plus-quadruple model” calculation, as a then most advanced many-body calculation, and advocated the “preponderance of axially symmetric shapes” over many species of nuclei. A similar work was reported by Bes and Sorensen [14]. These works indicated that once many nucleons in many single-particle orbits of a mean potential coherently contribute, the axially-symmetric prolate deformation likely occur. The SU(3) model is a symmetry based many-body approach, and favors the same feature [15, 16], as well as its approximate extensions [17].

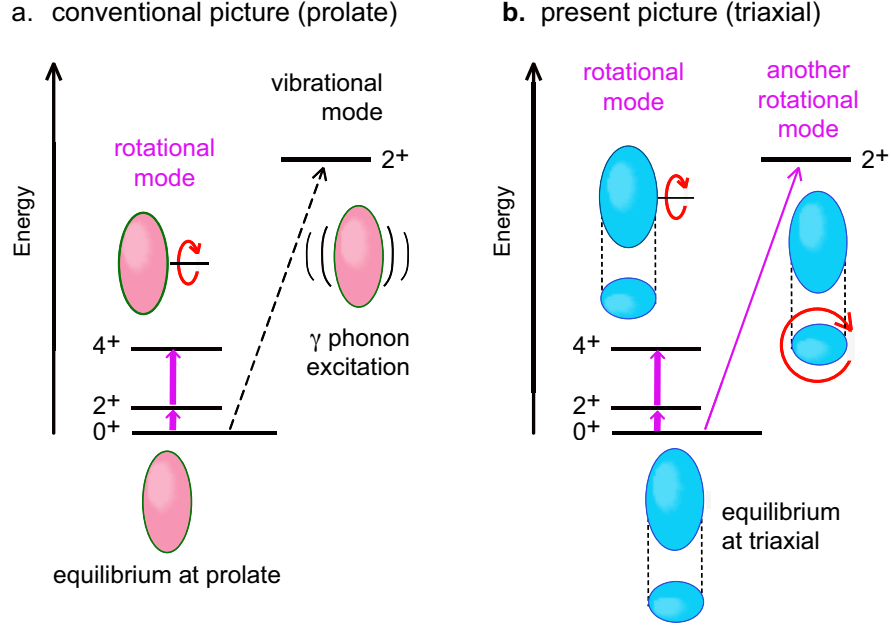
Figure 3a shows a schematic picture of the prolate deformed ground state and its rotational excitations. Figure 3a

includes another type of excitation, called γ vibration [1, 4]. This excitation stands for a vibrational excitation of the circle in Fig. 1c, f, represented by γ phonon. The 2^+_2 state is then identified as the one- γ -phonon state on top of the deformed equilibrium [1, 4] (see Fig. 3a).

Figure 3c depicts measured excitation energies as well as electromagnetic decays and moments [18], for ^{166}Er as an example of observed deformed nuclei. The decays are actually electric quadrupole (E2) transitions, and their strengths are expressed by squared E2 strengths called $B(E2; J^+ \rightarrow J'^+)$. The 2^+_2 state decays to the ground state through relatively strong transition with $B(E2; 2^+_2 \rightarrow 0^+_1) = 5.17 \pm 0.21$ (W.u.) (see panel c), where W.u. implies the single-particle (Weisskopf) unit [19]. Such somewhat large $B(E2)$ value was interpreted as an indication that the 2^+_2 state is indeed a phonon excitation which is collective to a certain extent.

III. MULTI-NUCLEON STRUCTURE BY CONFIGURATION INTERACTION SIMULATION

We present a recent work on this subject from a modern viewpoint combined with state-of-the-art configuration interaction (CI) calculations with a realistic effective nucleon-nucleon (NN) interaction. The CI calculation in nuclear physics is called *shell model*, and some introductory details



c. level energies and E2 properties of ^{166}Er

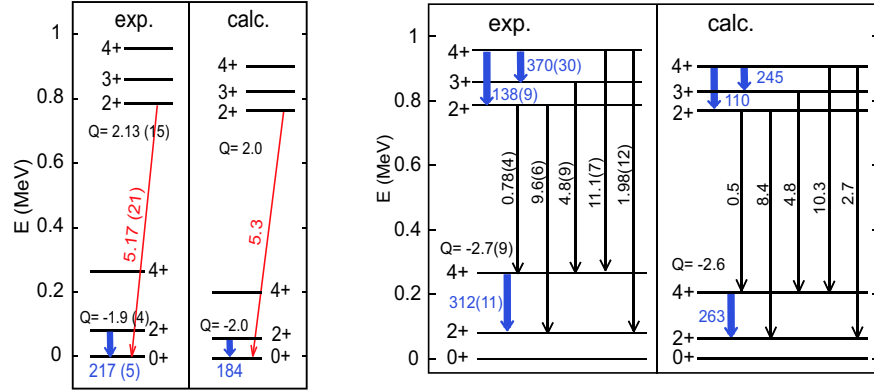


FIG. 3. Schematic pictures of rotational motion and actual features. **a** Conventional picture (prolate shape) and γ vibration from it. **b** Present picture (triaxial shape). **c** Levels and E2 properties of ^{166}Er compared to experimental data [18]. B(E2) values are in W.u., and spectroscopic electric quadrupole moments, Q, are in e barn.

are found in Appendix A. The CI calculation here means Monte Carlo Shell Model (MCSM) [20–23], which enabled us to carry out CI calculations far beyond the limit of the conventional CI approaches, on contemporary challenges [24–34]. Some details of the MCSM are presented in Appendix B. A large number of single-particle orbits are taken so that the ellipsoidal deformation can be described, 8 for protons and 10 for neutrons. The nucleus ^{166}Er is mainly discussed as an example, with 28 active protons and 28 active neutrons. The present work goes far beyond the earlier paper [30], by clarifying the fundamental robust mechanism, by covering a wider range of nuclei, and by looking for future impacts. The present CI calculation is carried out by the most advanced methodology using the number-projected quasiparticle vacua for the MCSM basis vectors instead of Slater determinants,

which can be specified as the Quasiparticle Vacua Shell Model (QVSM) [35].

A prototype of the present Hamiltonian was obtained and used in the earlier work [30]. The proton-neutron (interaction) part was obtained from the monopole-based-universal interaction, V_{MU} [36], which was derived based on the shell-model and microscopic interactions [36] and has been used in many studies, up to Hg isotopes [27]. The proton-proton and neutron-neutron interactions were fixed in Ref. [30] mainly based on the microscopic interactions used in Ref. [37]. In the earlier work, the pairing correlations in wave functions can be underestimated because of the Slater-determinant expansion in the original MCSM, and its strengths were likely taken to be stronger, in order to compensate this possible underestimation in reproducing experimental data. This problem vanishes

in the present calculation to a large extent, and the pairing strengths are rescaled to be somewhat weaker. The SPE values are also changed slightly. Overall features of the outcome do not change from the earlier work [30], while a larger number of nuclei, beside ^{166}Er , are studied in the present study.

Figure 3c depicts calculated level energies and E2 properties of ^{166}Er , in a good agreement with experiment, including both large and small values of $B(E2)$. The present value of $B(E2; 2_2^+ \rightarrow 0_1^+)$ is 5.3 W.u. in a salient agreement with experiment, and urges us to look into underlying multi-nucleon structure of the eigenstates.

For this purpose, deformation parameters β_2 and γ are introduced [1] to indicate how the sphere with the radius R_0 is deformed. The β_2 parameter (typically ~ 0.3) denotes the degree of deformation. The γ parameter is an angle related to the ratio between R_x and R_y . They are mutually linked as (see Fig. 1e),

$$R_z = \{1 + 0.63\beta_2 \cos \gamma\} R_0, \quad (1)$$

$$R_x = \{1 + 0.63\beta_2 \sin(\gamma - 30^\circ)\} R_0, \quad (2)$$

$$R_y = \{1 - 0.63\beta_2 \cos(60^\circ - \gamma)\} R_0. \quad (3)$$

Prolate shapes ($R_x=R_y$) correspond to $\gamma=0$, while triaxial shapes emerge for $0^\circ < \gamma < 60^\circ$. Usually, $\beta_2 \geq 0$ and $0^\circ \leq \gamma \leq 60^\circ$ are considered, implying $R_y \leq R_x \leq R_z$. The β_2 and γ parameters for a quantum state can be obtained by evaluating quadrupole moments Q_0 and Q_2 [38, 39]), and by calculating $R_{x,y,z}$ values of the afore-mentioned uniform ellipsoid having the same Q_0 and Q_2 values.

A constrained mean-field (more concretely Hartree-Fock-Bogoliubov) calculation is carried out by imposing various values of (β_2, γ) as constraints. The obtained energy expectation value is displayed by contour plot in Fig. 4b, with a legend in Fig. 4a. This plot is usually called the potential energy surface (PES). The same Hamiltonian as the present CI, or MCSM, calculations is consistently used. The PES in Fig. 4b suggests that the bottom part of the PES spreads around a finite γ angle, and the precise inspection actually indicates that the minimum is not at $\gamma=0$ but around $\gamma \sim 9^\circ$. This contradicts the prolate preponderance hypothesis believed over seven decades. For $\gamma=9^\circ$, the values of $R_{x,y,z}/R_0$ are 0.93, 0.88 and 1.19, respectively.

The wave functions of the MCSM are expanded by so-called MCSM basis vectors, which are presently number-projected quasiparticle vacua [35]. These basis vectors are selected from a large group of candidates generated stochastically, so that the maximum possible lowering of the energy eigenvalues of interest can be obtained. The selected basis vectors are further optimized by variational procedures [20]. Some details of the computational methodology are presented in Appendix B. Each of basis vectors has intrinsic quadrupole moments, from which the corresponding (β_2, γ) value is obtained. The individual basis vector can be represented by a circle pinned down on the PES according to this (β_2, γ) value, which now serves as a “partial labelling” of the basis vector.

The importance of each basis is depicted by circle’s area proportional to the overlap probability with the eigenstate. This visualization is called T-plot [40], and turned out to be very useful (see Appendix B).

Figure 4c displays the T-plots for the 0_1^+ , 2_1^+ , 4_1^+ states (ground-band members), and the 2_2^+ , 3_1^+ , 4_2^+ states (so-called γ -band members), as well as the 4_3^+ state. All of them exhibit remarkably similar T-plot patterns, *i.e.*, the mean position and fluctuation. This similarity suggests a rather common triaxiality among these states, which is consistent with the picture shown in Figure 3b: all these states can be generated, to a good extent, by rotating a common triaxial ellipsoidal state in multiple ways.

The mean value of γ is evaluated [39] to be 8.2° for 0_1^+ , 2_1^+ , 4_1^+ , 9.1° for 2_2^+ , 3_1^+ , 4_2^+ , and 9.5° for 4_3^+ , where small variations (beyond two digits) are not shown. These values are almost the same, and in particular, are almost exactly so within a band. This fact suggests that a fixed triaxial shape governs ^{166}Er . This property holds up to the 4_3^+ state, where the CI calculation stopped due to the computer resource.

The mean value of γ is about 1° larger for the γ band than for the ground band. This difference reflects structure changes from the ground band to the γ band, and its impact on the relative energy between these two bands is of great interest. While the energy of the 0_1^+ state is calculated with many basis vectors (see Appendix B for details), the first basis vector, denoted ξ_0 here (ϕ_1 in eq. (B1) for 0_1^+), is most important among them: it indeed shows a large overlap probability with the final solution, 89% after the projections and normalization. We next look at the 3_1^+ member of the γ band. This state has no counterpart in the ground band and should well represent features of the γ band. We first calculate its energy by using ξ_0 alone, similarly to the 0_1^+ state. Although the obtained energy of 3_1^+ state is not too bad, its difference from the 0_1^+ -state value is 1.27 MeV, which is notably larger than the result shown in Fig. 3c, that is 0.83 MeV. However, instead of ξ_0 , by using another state, ξ_3 , determined by solely lowering the energy of the 3_1^+ state, the obtained 3_1^+ state comes down from 1.27 MeV to 0.76 MeV above the 0_1^+ state obtained from ξ_0 , apparently closer to the result in Fig. 3c. The overlap probability with the final solution becomes as high as 88%. Thus, the most optimum basis vector is slightly different between the 0_1^+ and 3_1^+ states. By including additional basis vectors into the actual MCSM calculation, the energies of the 0_1^+ and 3_1^+ states come down, and their difference swiftly reaches the value shown in Fig. 3c.

The value of γ is 8.5° and 9.8° for ξ_0 and ξ_3 , respectively, being similar to the mean γ values of the ground and γ bands. The analysis above indicates that this difference lowers the γ -band excitation energy by ~ 0.5 MeV. Once this lowering occurs, additional basis vectors do not substantially change the γ -band excitation energy, with a 0.07 MeV shift in the final solution. These features suggest that the γ -band excitation energy is substantially lowered due to the enlargement of the triaxial deformation. We stress that this effect is due to NN interactions incorporated into the MCSM calculation.

The rotation shown in the lower-right corner of Fig. 1d is interpreted to approximately carry spin 0, 2 and 4, respec-

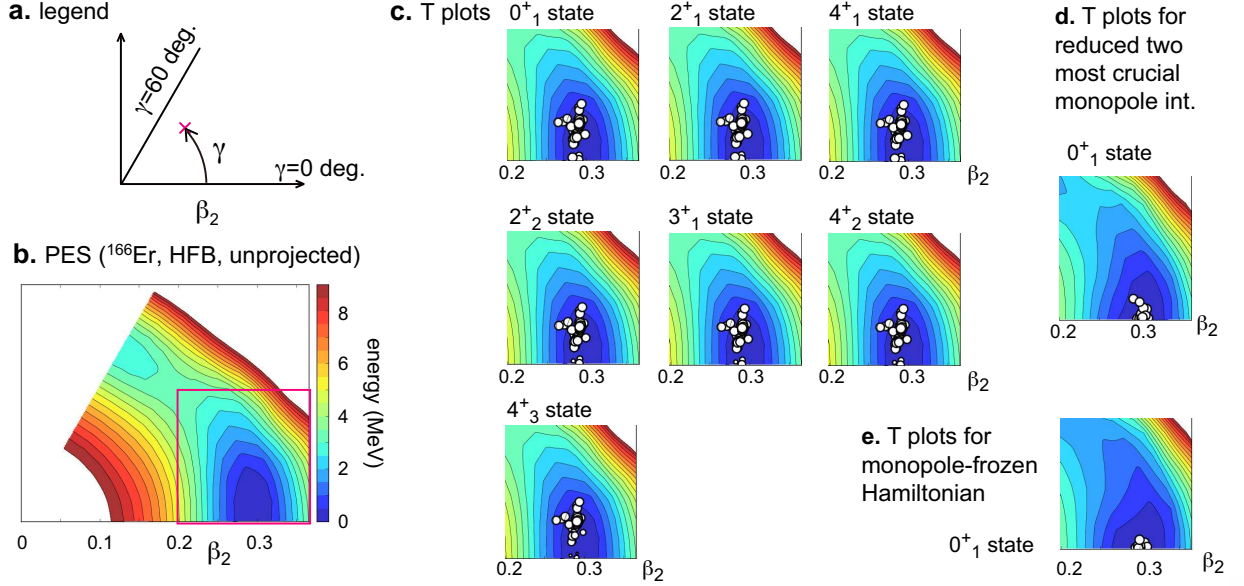


FIG. 4. PES and T-plots for ^{166}Er **a.** Legend. **b** PES. **c** T-plots of ground and low-lying states for the red-square region of **b**. All T-plots are independently obtained, despite resulting resemblances. **d** T-plots for reduced crucial monopole interactions. **e** T-plots for monopole-frozen Hamiltonian.

tively, for the $(0_1^+, 2_1^+, 4_1^+)$, $(2_2^+, 3_1^+, 4_2^+)$, and 4_3^+ states. It corresponds to so-called K quantum number. The vector coupling with the other rotation in Fig. 1d forms the total spin of the nucleus. The K quantum number is approximately conserved in the present case as the actual γ value is well below 15° . This is well known feature, for instance [41], and is discussed for ^{166}Er in Ref. [42].

Based on the afore-mentioned identification of the K quantum number, the enlargement of the γ angle from the ground to the γ band can be interpreted as a kind of the centrifugal effect that distorts more the ellipse in the right-lower part of Fig. 1d. The deformation along the longest (or vertical) axis in the left part of Fig. 1d is considered to be more stable corresponding to a strong binding mechanism, and creates practically perfect rotors not only within the ground band but also within the γ band. The deformation perpendicular to this axis, however, appears to increase (or γ increases) for K higher. Because of this “stretching”, the excitation energies associated with the K quantum number are lowered due to enlarged moment of inertia, as seen in the experiment and also in the present MCSM calculation. Consistently with the stretching picture, the γ band depicts, as compared to the ground band, the weakening (enlargement) of the 0^+ -pairing (2^+ -pairing) correlation, as well as enhanced effect of the proton-neutron interaction, which is the origin of deformed shapes (see Fig. 2a) [43].

Note that the vibrational-excitation picture was critically assessed from more general viewpoints in Refs. [44, 45].

IV. DOUBLE GAMMA PHONON STATE

We comment on the calculated 4_3^+ state. There might be other 4^+ state(s) below this state, but we just focus on this. The

4_3^+ state appears to correspond to the observed state with an interpretation as the $\gamma\gamma$ 4^+ state, a state with double γ phonon excitations in the traditional picture [46, 47]. A simple estimation of its level energy is twice that of the γ phonon 2^+ state, 2×0.79 MeV for ^{166}Er . Its experimental candidate state has been observed at substantially higher energy, 2.03 MeV (see Refs. [18, 42, 46, 47]). This discrepancy has attracted attentions.

The present theoretical 4_3^+ state is a higher member of almost the same triaxial shape with the so-called K quantum number ~ 4 , as shown in the right part of Fig. 1d (see Ref. [42]). It is more triaxial as shown in Fig. 4c. The calculated excitation energy of this state is 2.22 MeV, being closer to the observed value, 2.03 MeV (see Refs. [18, 46, 47]). The calculated value $B(E2; 4^+ \rightarrow 2_2^+) = 10.4$ W.u. is also in agreement with its experimental value 8 ± 3 W.u. [18].

V. DAVYDOV MODEL

The model with rigid and triaxial shape was intensively discussed in 1958 by Davydov and his collaborators [48, 49]. For $\gamma = 9^\circ$, the ratio $B(E2; 2_2^+ \rightarrow 0_1^+)/B(E2; 2_1^+ \rightarrow 0_1^+)$ is 0.0238 in this Davydov model [42], in agreement with the experiment and the present calculation (see Fig. 3c). As electromagnetic properties directly scan the shapes, the Davydov model appears to be consistent with the present scheme for the shapes. Excitation energies are another story, however. The experimental ratio $E_x(2_2^+)/E_x(2_1^+)$ is 9.8. The Davydov model yields ~ 20 for $\gamma = 9^\circ$, and requires $\gamma \sim 14^\circ$ to reproduce this experimental value. Thus, the Davydov model shows inconsistency within the model. The present CI calculation, in contrast, incorporates variable triaxiality, which indeed changes more

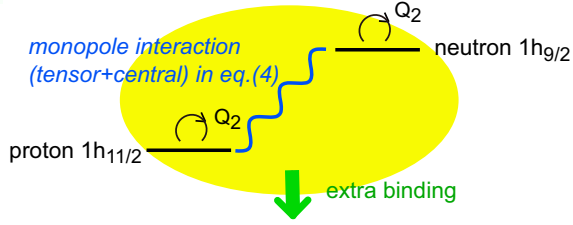


FIG. 5. Mechanism making triaxial ground and low-lying states. The blue wavy line indicates monopole interaction which is particularly strongly attractive due to coherent contribution from tensor and central nuclear forces. The enhancement of the Q_2 quadrupole moment is indicated by round arrows.

or less from band to another, and possibly other effects, and reproduces the γ -band excitation energy, as discussed above. The Davydov model is simply too rigid to handle such effects, but the concept of triaxial shapes appears to be appropriate.

We note that the deformed shell model by Sun *et al.* [45, 50], was applied, with assumed triaxiality, to a number of heavy nuclei.

VI. MONOPOLE INTERACTION AND TENSOR FORCE

It is of interest and importance to find the origin of the present triaxiality in nuclear forces. A crucial key here is the monopole interaction (see a review in [51]), which is a part of any two-body interaction (see Ref. [52] for concise description). When two nucleons are in single-particle orbitals j and j' , the orbital motions occur about the corresponding axes. The monopole interaction stands for an averaged effect taken over all possible axis orientations, for a given interaction. The monopole interaction between a proton and a neutron is expressed as [51, 52]

$$v_{mono} = \sum_{j,j'} v_{j,j'}^{mono} n_j^{(p)} n_{j'}^{(n)} \quad (4)$$

where $n_j^{(p)}$ ($n_{j'}^{(n)}$) denotes the number of protons in orbital j (neutrons in j'), and $v_{j,j'}^{mono}$ is the coefficient called monopole matrix element. The neutron single-particle energy (SPE) of the orbital j' is effectively shifted by $\sum_j v_{j,j'}^{mono} n_j^{(p)}$ or vice versa. Evidently, these effects of monopole interaction are configuration dependent, or dynamically vary. If the monopole interaction is particularly strong (or $v_{j,j'}^{mono}$ is large) between specific j and j' , it can have crucial impacts on the nuclear structure.

The monopole interaction of the tensor force brings about such impacts [51, 53]. It generates a strong attraction, for instance, between a proton in the $j = l + 1/2$ orbital and a neutron in the $j' = l' - 1/2$ orbital, where j and j' (l and l') denote the total (orbital) angular momenta, and $1/2$ implies the intrinsic spin of a nucleon. Note that j also means the index of the orbital. The monopole interaction of the tensor force is indeed strongly attractive between the proton $1h_{11/2}$ orbital and the neutron $1h_{9/2}$ orbital with $v_{1h_{11/2}, 1h_{9/2}}^{mono} = -0.08$ MeV. Combined with the contribution from the central force

[36], the total monopole interaction becomes strongly attractive with $v_{1h_{11/2}, 1h_{9/2}}^{mono} = -0.39$ MeV, well beyond the average value of $v_{j,j'}^{mono}$, -0.25 MeV over all orbitals. The tensor force contribution is more than half the extra gain (see Fig. 5). As the monopole effect is linearly dependent on $n_j^{(p)}$ and $n_{j'}^{(n)}$ (see eq. (4)), its magnitude can be multiplied by a factor 10 or more. This is a unique property absent in any part of the interaction but the monopole. The monopole interaction between two protons or between two neutrons is not so relevant here.

The tensor force is a part of the nuclear forces. After the prediction of meson mediated nuclear forces by Yukawa [54], Bethe formulated the tensor force [55]. If one π meson is emitted from a nucleon and is absorbed by another nucleon, a tensor force arises between these two nucleons. In other words, the one- π -exchange process and a tensor force are the same thing to a great extent. This is the major origin of the tensor force working between nucleons, with the cancellation by about a quarter due to ρ meson exchange, a resonance of two π mesons. The proton-neutron interaction is given by the V_{MU} interaction as mentioned earlier, and this interaction includes these tensor forces with strengths evaluated in Ref. [56]. The NN interaction acting on nucleons bound in nuclei undergoes substantial renormalization in general, and is changed. It was shown, however, that the tensor force, particularly its monopole interaction, remains rather unchanged. This unique property is referred to as the renormalization persistency [57]. Thus, the π meson exchange is the major origin of the tensor force in nuclei.

VII. MECHANISM OF THE ENLARGEMENT OF Q_2 MOMENT

We here discuss basic mechanisms of the appearance of triaxiality in the present case, in a pedagogical way using schematic examples. The single-particle orbitals in the harmonic oscillator potential are degenerate if they belong to the same oscillator quanta. Figure 6a shows one of such cases (the oscillator quanta = 5, comprising $1h_{11/2,9/2}$, $2f_{7/2,5/2}$ and $3p_{3/2,1/2}$ orbitals). If a quadrupole deformation sets in as Fig. 2a exhibits, it is known that a prolate shape, which is axially-symmetric, arises in the ground and low-lying states, and this feature remains if the degeneracy is lifted (or loosened) to a certain extent, as shown in early studies [13, 14], leading to the preponderance of axially-symmetric prolate shapes. A similar situation occurs with the SU(3) symmetry [15, 16]. Another work showing the dominance of the prolate nuclear shapes was a systematic survey in terms of the Skyrme Hartree-Fock calculation [58]. The result appeared to be consistent with the above-mentioned other works. The universal finite-range liquid-drop model (FRLDM) similarly predicts no triaxial ground states for the deformed nuclei discussed in this article (see Fig. 2 of Ref. [59]).

This has been the conventional picture for the deformed nuclear shapes, but a different picture now emerges for heavier nuclei. Figure 6b exhibits an illustrative example focusing on the lowering of the $1h_{11/2}$ orbital. This lowering is partly due to a typical phenomenon in nuclei. The orbitals of large

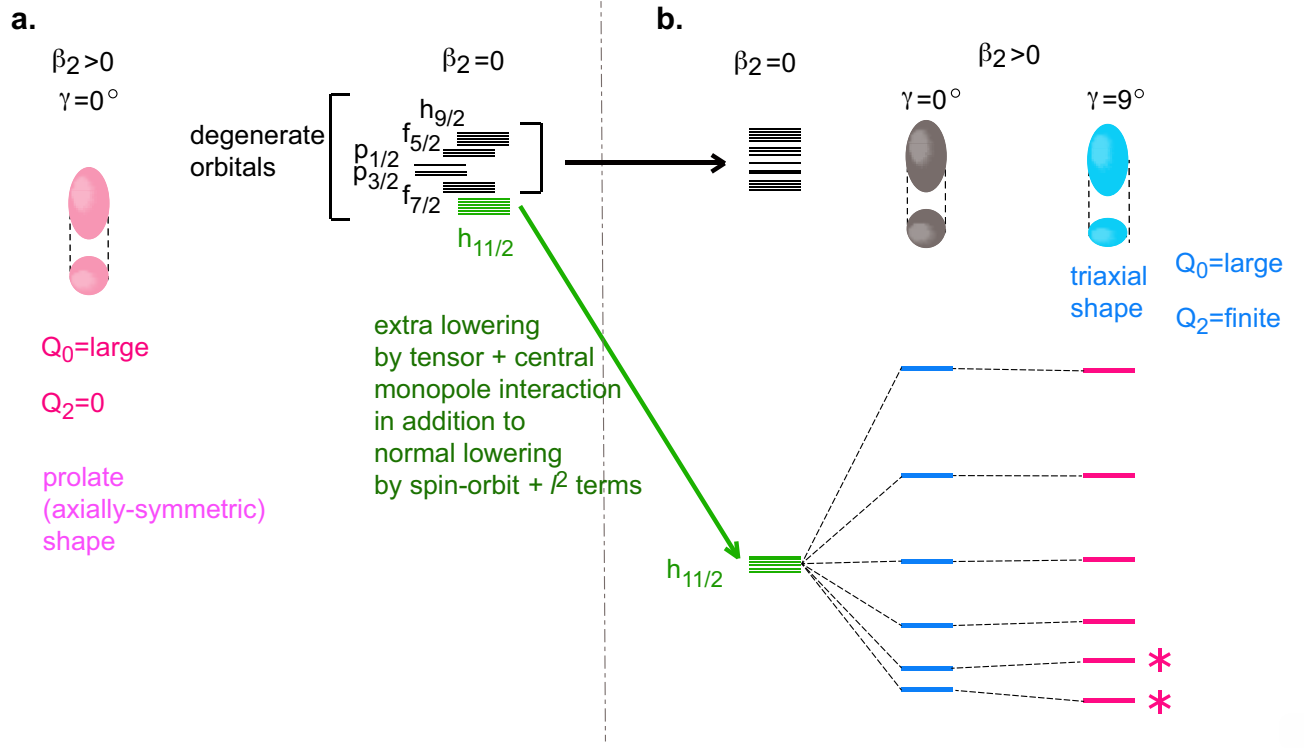


FIG. 6. Triaxiality development in single-particle orbital $h_{11/2}$. **a** Prolate case ($\gamma=0$) with degenerate single-particle orbitals. **b** Splitting and mixing of single-particle states of the $h_{11/2}$ orbital shown by blue ($\gamma=0$) and red ($\gamma=9^\circ$) horizontal bars. The red asterisks imply that the occupation of these states can generate the triaxiality (or finite Q_2).

$j = l + 1/2$ are shifted down in energy due to the spin-orbit splitting and the so-called l^2 term which are stronger for larger l values [19]. This effect was included in earlier studies such as Refs. [13, 14], and does not change the preponderance of prolate shapes. There is another effect, however. As graphically shown in Fig. 5, an extra attraction emerges, for instance, between the proton $1h_{11/2}$ orbital and the neutron $1h_{9/2}$ orbital.

Figure 6b exhibits that the energies of single-particle states of the $1h_{11/2}$ orbital in the body-fixed frame, for z -component of j : $j_z = \pm 1/2, \pm 3/2, \dots, \pm 11/2$. For $\beta_2 = 0$, the nucleus is spherical, and the energies of these single-particle states are degenerate (see below $\beta_2 = 0$). Once the nucleus is deformed, this degeneracy is lifted. For a prolate ellipsoid (in gray) with $\beta_2 > 0$ and $\gamma = 0$, the j_z quantum number is conserved in each single-particle state. The energies of these states are split in the ascending order, $j_z = \pm 1/2, \pm 3/2, \dots, \pm 11/2$. The degeneracy between positive and negative signs is due to the time reversal symmetry.

There are sizable matrix elements of the Q_2 moment, for instance, between the states of $j_z = 1/2$ and $5/2$, as the Q_2 operator can change the j_z by two units. The single-particle states of different j_z 's are mixed in the eigenstates of a quadrupole field involving certain triaxiality ($\gamma \neq 0$). Such eigenstates then yield non-vanishing Q_2 moments. These Q_2 moments are coupled with the Q_2 deformed field (produced by other nucleons), shifting the energies. Such energy shifts are depicted, for $\gamma = 9^\circ$ in the far right column of Fig. 6b. The lowest state shows extra binding energy. If the lowest state or the

two lowest states, marked with asterisks, are occupied, certain Q_2 moments are produced, driving the nucleus into triaxial shape. This is one of the basic mechanisms to yield finite Q_2 moment, or triaxial shape.

Figure 6b indicates that the lowering of $1h_{11/2}$ orbitals leaves an incomplete harmonic oscillator shell. As stated above, the Q_2 moment of the nucleus is zero or small in magnitude for strongly deformed states, if all orbitals of a harmonic oscillator shell are degenerate or almost so. As individual matrix elements of the Q_2 operator are not small, the cancellation should occur among individual effects. With the $h_{11/2}$ orbital separated from the rest of the orbitals, this cancellation becomes less perfect, which results in another source of finite Q_2 moment.

Figure 6b suggests that two to four nucleons in high- j orbitals can substantially contribute to Q_2 moment. Regarding ^{166}Er , this occurs in the combination (proton $1h_{11/2}$, neutron $1h_{9/2}$) and in the combination (proton $1g_{7/2}$, neutron $1i_{13/2}$), because they are populated by more nucleons due to strongly attractive proton-neutron monopole interactions, $v_{1h_{11/2}, 1h_{9/2}}^{\text{mono}}$ and $v_{1g_{7/2}, 1i_{13/2}}^{\text{mono}}$. Note that the proton $1g_{7/2}$ orbital contributes to the monopole effect but not to Q_2 moment, as it is nearly fully occupied.

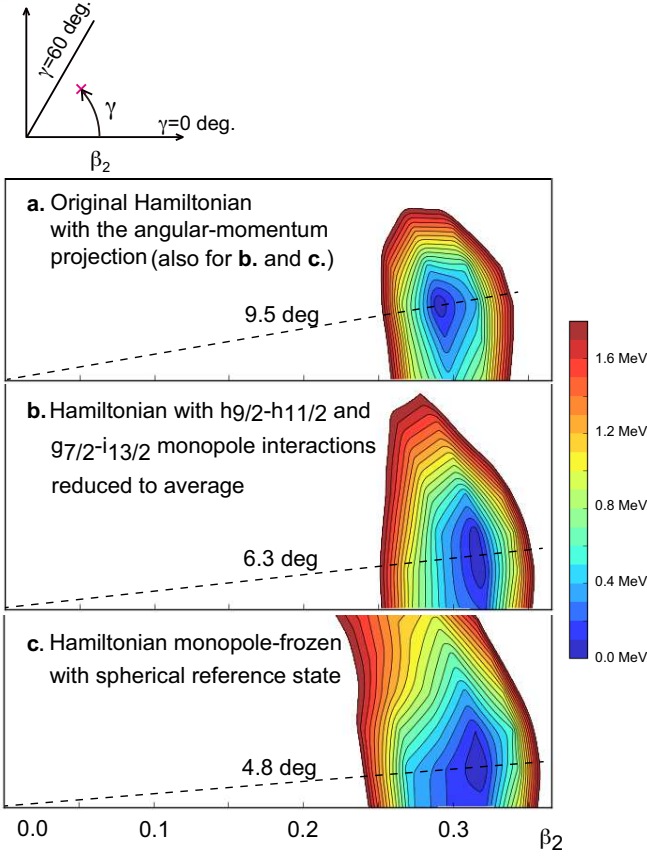


FIG. 7. PES near the minimum by the constrained HFB after the projection on to $J^P=0^+$. The calculations are made with **a** the original Hamiltonian, **b** the Hamiltonian where two crucial monopole interactions are reduced, **c** the Hamiltonian monopole-frozen with spherical HFB reference state. Dashed lines are drawn to show representative γ angles.

VIII. ANALYSES WITH REDUCED OR ELIMINATED MONOPOLE INTERACTIONS

This monopole-quadrupole combined effect naturally occurs in the actual CI wave functions, and provide more binding energies to triaxial states over prolate states, making triaxial ground and low-lying states. We look into this effect with two analyses.

A. Analysis with reduced monopole interactions

In order to confirm this effect, $v_{1h_{11/2}, 1h_{9/2}}^{mono}$ and $v_{1g_{7/2}, 1i_{13/2}}^{mono}$ are reduced to the average value, -0.25 MeV (see Sec. VI). Figure 7 displays details of the PES near the minimum. The PES minimum of the original Hamiltonian (panel **a**) is located at $\gamma=9.5^\circ$ and its energy is lower by ~ 0.4 MeV than the lowest prolate point. Panel **b** shows the result of this monopole-reduced Hamiltonian: the minimum at $\gamma=6.3^\circ$ is only ~ 0.1 MeV below the prolate minimum. The T-plot is

more striking as shown in Fig. 4d, which depicts a strong concentration of T-plot circles towards a prolate shape. Thus, instead of conventionally conceived mechanism (see Fig. 3a), another one in Fig. 3b emerges for the original Hamiltonian with realistic monopole interactions. The CI results indicate that the ground state of ^{166}Er contains about four protons in $1h_{11/2}$ and about four neutrons in $1h_{9/2}$, with which a strong quadrupole deformation with triaxiality is generated, and the extra monopole effect beyond the average one reaches about $-0.14 \times 4 \times 4 = -2.24$ MeV, a substantial additional binding. A similar but weaker effect arises from the (proton $1g_{7/2}$, neutron $1i_{13/2}$) combination.

The monopole interaction favors no specific shape, but can yield crucial effects for nuclear shapes by effectively changing single-particle energies in configuration-dependent manners. This mechanism is referred to, in general, as the self-organization [30, 52]. In the case of ^{166}Er , certain configurations favoring triaxiality gain more binding energy due to this mechanism.

For the mechanism of the triaxiality, it is crucial to put proper numbers of nucleons in the relevant large- j orbitals. If they are too few or too many (like the prolate case of Ref. [27]), the Q_2 moment cannot be large enough, and the shape moves to a spherical or a prolate one.

B. Frozen Analysis

As another way to see the crucial contribution of the monopole interaction, we calculate mean shifts of the SPEs by taking expectation values of $n_j^{(p)}$ etc. in eq. (4) with a reference state. We then remove the monopole interaction and instead include such mean shifts of the SPEs. Namely, dynamical effects of the monopole interaction are *frozen* with this reference state [30]. The CI calculation is then performed. In this work, a spherical state, given by constrained HFB calculations, is used as the reference state. Fig. 7c includes PES of this monopole-frozen Hamiltonian. The minimum is closer to the prolate minimum than in panels **a, b**. Figure 4e displays the T-plot of the 0_1^+ state obtained by the present monopole-frozen Hamiltonian. The strong deformation remains, but the triaxiality disappears. This further confirms that the activation of the monopole interaction is crucial for the triaxiality.

IX. NUCLEI AROUND ^{166}Er IN THE SEGRÈ CHART

The CI calculations shown here require huge computer resources, and thereby we have performed them for ^{162}Er , ^{164}Dy and ^{158}Gd besides ^{166}Er . These nuclei show similar structure and triaxiality. One of the signatures of the triaxiality is the 2_2^+ level below the 0_2^+ level. Figure 8 displays a part of the Segrè (nuclear) chart (even-even nuclei around ^{166}Er), where star symbols indicate deformed nuclei ($E_x(2_1^+) < 0.15$ MeV) with this signature from experiment [6, 18]. As the nuclei shown by red star symbols are traditionally supposed to have prolate ground states, the overall picture of nuclear shape is drastically changed. The purple star symbols form a separate

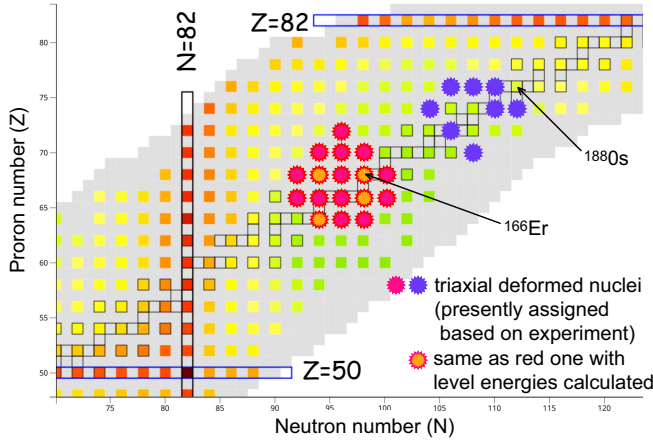


FIG. 8. Nuclear chart (part) and triaxially deformed nuclei (red and purple star symbols). Red squares indicate the lowest 2^+ states with higher level energies (> 1 MeV), while green ones stand for those with lower level energies (< 0.1 MeV). The colors in between indicate intermediate cases. Background given by NuDat 3.0 [6].

group, some of which were considered to be triaxial, as its neighbor, ^{188}Os was considered to have $\gamma=30^\circ$ (Ref. [60]). Missing star symbols do not necessarily imply prolate shapes but rather mean unavailable experimental data. The present calculation is consistent with these features (See Figs. 9 and 10).

The Hamiltonian used for ^{166}Er appears to work well for other nuclei such as ^{162}Er , ^{164}Dy , ^{158}Gd and ^{170}Er , as shown in Fig. 9 a-e. These panels show not only the level energies but also the values of $B(E2; 2_1^+ \rightarrow 0_1^+)$, $B(E2; 2_2^+ \rightarrow 0_1^+)$ (in W.u.) and spectroscopic electric quadrupole moments (in e barn). A good agreement to experiment [18] is visible. As an example, the 2_2^+ , 3_1^+ and 4_2^+ states of ^{162}Er (panel b) are shifted upwards by the almost same amounts between theory and experiment, compared to those of ^{166}Er (panel a). A further shift is seen in ^{158}Gd similarly between experiment and theory (panels a and d). All shown levels remain quite unchanged between ^{164}Dy and ^{166}Er (panels a and c), but the $B(E2; 2_2^+ \rightarrow 0_1^+)$ value differs between these two nuclei also similarly in both theory and experiment. Thus, a good overall agreement is obtained between theory and experiment. In particular, the $B(E2; 2_2^+ \rightarrow 0_1^+)$ value changes by up to a factor of two from nucleus to nucleus, and the present calculation exhibits this variation rather well.

In the level scheme of ^{170}Er , the calculated 0_2^+ level is lower than the 2^+ levels except for the 2_1^+ level, excluding this nucleus from the group of the triaxiality.

All these features suggest the validity of the present Hamiltonian.

In addition, the PES of the nuclei shown by red star symbols in Fig. 8 are shown in Fig. 10, as well as some nuclei around them. The calculated PES depicts a trend consistent with the triaxial assignment in Fig. 8.

X. SUMMARY, PROSPECT AND A NOTE ON DAVYDOV

An unexpected role of the tensor force is found for the ellipsoidal nuclear shapes. The tensor force represents a major part of the π -meson exchange effects, and was shown to be responsible for the shell evolution in exotic nuclei [51–53], giving rise to new magic numbers (see Fig. 2). The shell structure becomes invisible in most of heavier nuclei as single-particle orbitals are mixed due to strong deformation. In these nuclei, the tensor force can produce completely different but still important effects towards triaxiality, through a quantum mechanical way of the self-organization [30]. Thus, the tensor force produces the shell evolution in exotic nuclei and the triaxial shapes in heavy deformed nuclei. Due to the renormalization persistency [57], the tensor force is the major consequence of the exchange of one π meson, being rather free from in-medium corrections, and we now see the direct connections between such an “elementary-particle” process and basic nuclear shapes. These findings make the trend towards triaxiality quite robust. The π -meson exchange is treated separately also in the modern theory of nuclear forces [61] as materialized as the chiral Effective Field Theory [62] of the Quantum Chromodynamics.

On top of the triaxiality due to the monopole-quadrupole interplay, the excitation energy of the γ band is lowered as the triaxiality further grows, like a stretching effect in the R_x direction of Fig. 1g.

It is a major experimental challenge to observe the triaxial shape. Magnetic excitation is a possibility: another mode may appear besides the scissors mode [63], as a contra oscillation between the proton and neutron ellipses about the longest axis (see the right-lower part of Fig. 1d), which may be called a rolling mode. Another intriguing possibility lies in relativistic heavy-ion collision as a new tool for scanning the nuclear shape [64]. The former experiment may be done in facilities like HIγS and RCNP, while the latter in LHC/CERN or RHIC. Another relevant feature is the chirality. As a result of substantial triaxiality in the strongly deformed region, nuclear chiral doublet bands [65] may appear more widely than expected, providing new experimental opportunities.

The binding energy gain by the deformation is likely more crucial in heavy and superheavy nuclei, and possible appearance of triaxiality was shown even without including the present mechanism, for instance, Ref. [66]. The triaxiality has also been addressed over decades as it may lower the first fission barrier [67]. As the triaxiality is a robust reality rather than an accidental incident, it may produce more visible effects on these nuclei than previously expected.

We finally note that the preponderance of triaxiality in heavy nuclei was suggested by a Ukrainian physicist, Dr. A. S. Davydov (Crimea 1912 - Kyiv 1993), but this suggestion has not been well appreciated due to some reasons. Since the basic idea is shown to be relevant, he and his work can be better appreciated.

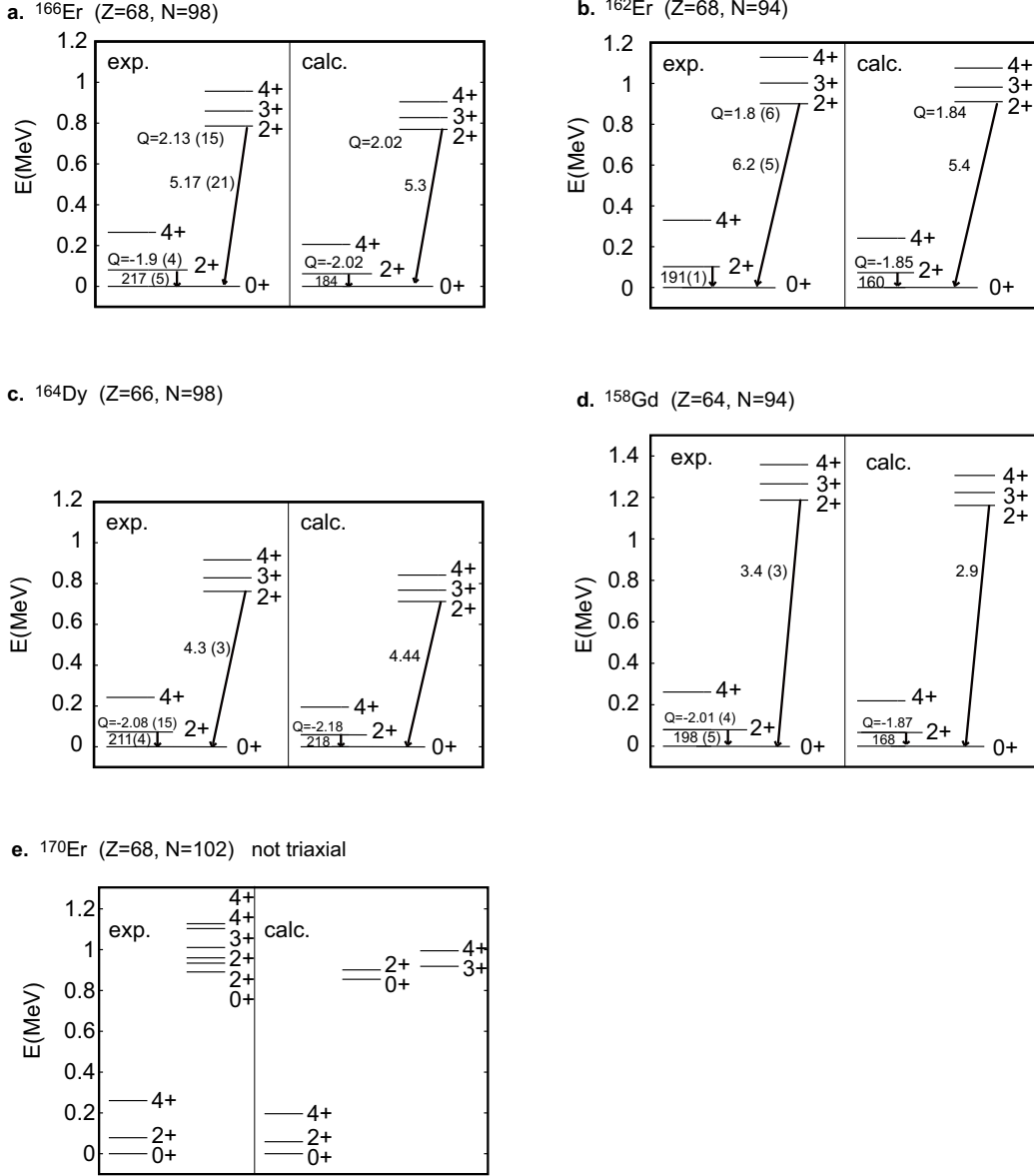


FIG. 9. Lowest level energies of triaxial nuclei. Selected triaxial nuclei are **a** ^{166}Er , **b** ^{162}Er , **c** ^{164}Dy and **d** ^{158}Gd . **e** Lowest level energies of a prolate nucleus, ^{170}Er , are depicted for comparison. For these triaxial nuclei, theoretical and experimental [18] values of $B(E2; 2_1^+ \rightarrow 0_1^+)$ and $B(E2; 2_2^+ \rightarrow 0_1^+)$ (see arrows) are shown in W.u. The spectroscopic electric quadrupole moment is shown (see "Q") in the unit of e barn for the 2_1^+ and 2_2^+ states for some nuclei [18].

Acknowledgements

The authors are grateful to Drs. P. Van Duppen, N. Pietralla, P. von Neumann-Cosel, A. Tamii, G. Giacalone, K. Nishio, Y. Aritomo, T. Azuma and S. Yamamoto for valuable suggestions and/or discussions. The MCSM calculations were performed on the supercomputer Fugaku at RIKEN AICS (hp190160, hp200130, hp210165, hp220174). This work was supported in part by MEXT as "Priority Issue on Post-K computer" (Elucidation of the Fundamental Laws and Evolution of the Universe) (hp160211, hp170230, hp180179, hp190160) and "Program for Promoting Researches on the

Supercomputer Fugaku" (Simulation for basic science: from fundamental laws of particles to creation of nuclei) (JP-MXP1020200105), and by JICFuS. This work was supported by JSPS KAKENHI Grant Numbers JP19H05145, JP21H00117, JP21K03564, JP20K03981, JP17K05433 and JP18H05462.

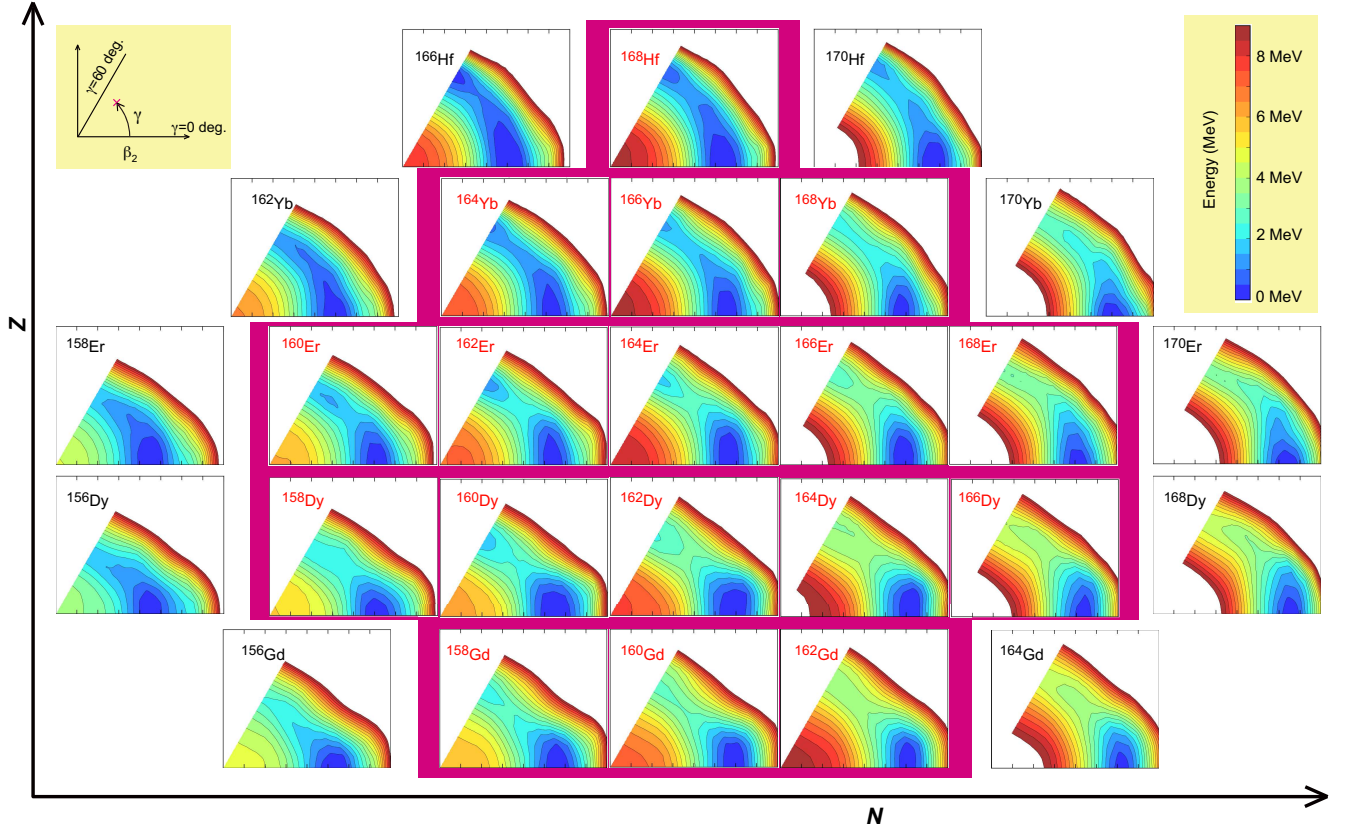


FIG. 10. PES of 17 triaxial deformed nuclei and their neighbors. The present deformed triaxial nuclei are in dark-pink background and are named in red. The neighboring nuclei are in blanc background and are named in black. The PES is calculated by the HFB calculation without angular-momentum projection. The particle numbers are projected.

Appendix A: Configuration Interaction (CI) calculation or Shell-model calculation

We sketch the shell model for atomic nuclei in this Appendix. The shell-model calculation is one of the standard methods for the nuclear many-body problem [9, 10, 17, 68]. It belongs to the category of the Configuration Interaction (CI) calculation, which is more familiar to broad audience and is also used in this article for the meaning of the shell model. The ingredients of the shell model are (i) single-particle orbitals and their energies, (ii) the numbers of protons and neutrons in these orbitals, (iii) nucleon-nucleon (NN) interaction. Thus, the properties of the nuclear states are determined by them, without other a priori assumption. The protons and neutrons can move in these orbitals, scattering each other through the NN interaction adopted. These protons and neutrons (collectively called nucleons) do not include the nucleons in the inert core, as it is a closed shell and is treated as the vacuum. The single-particle energies (SPE) and the NN interaction are taken from some models and/or theories. The matrix elements of the SPE and the NN interaction are expressed, as one- and two-body operators, respectively, with respect to all possible combinations of single-particle states, which are magnetic substates of each single-particle orbitals.

The Hamiltonian consists of one-body term and two-body

term, as usual. The one-body term is expressed by the SPEs, and the two-body term is expressed in terms of the matrix elements of the NN interaction with respect to antisymmetrized two-nucleon states. The Hamiltonian is thus constructed, and the actually used Hamiltonian is mentioned in the main text.

The many-body states are described by superpositions of Slater determinants in many *conventional* shell-model calculations. The many-body Schrödinger equation is solved for the given Hamiltonian as,

$$H\Psi = E\Psi, \quad (\text{A1})$$

where Ψ is an eigenstate for an eigenvalue E , and the Hamiltonian *matrix* for this many-body system is represented by matrix elements of the Hamiltonian *operator* for all combinations (bra and ket vectors) of all possible Slater determinants. By diagonalizing this Hamiltonian matrix, energy eigenvalues and wave functions of eigenstates are obtained. We can calculate various physical quantities from these wave functions. The number of Slater determinants is called shell model dimension. This is the general framework of the shell model, while many-body states can be equivalently expressed otherwise.

The shell model dimension becomes huge in many interesting cases, restricting the actual feasibility of the calculation. This is the major obstacle of the conventional shell-model cal-

culatation, and the current limit of the shell-model dimension is around 10^{11} as of 2019 [69]. In order to overcome this difficulty, the Monte Carlo Shell Model was introduced, as described in the next Appendix.

The practical setup of the present work is mentioned [30]. Proton single-particle orbitals are, $1g_{9/2,7/2}$, $2d_{5/2,3/2}$, $3s_{1/2}$, $1h_{11/2}$, $2f_{7/2}$, and $3p_{3/2}$. The neutron single-particle orbitals are, $1h_{11/2,9/2}$, $2f_{7/2,5/2}$, $3p_{3/2,1/2}$, $1i_{13/2}$, $2g_{9/2}$, $3d_{5/2}$ and $4s_{1/2}$. These orbitals define the model space, which is built on top of the $Z=40$ and $N=70$ magic numbers of the Harmonic Oscillator potential. In the case of ^{166}Er , 28 protons and 28 neutrons are put into the model space formed by these orbitals. The model space and the number of nucleons are much larger than those in the usual shell-model calculation, so that the shape deformation can be described. The shell-model dimension becomes as large as 4.8×10^{33} for the case of ^{166}Er . This is far beyond the limit of the conventional shell-model calculation, but can be overcome by using the MCSM described in the next Appendix.

Appendix B: Monte Carlo Shell Model and T-plot

In this Appendix, we briefly describe the Monte Carlo Shell Model (MCSM). The MCSM was initially proposed in Ref. [21]. A prototype of its present version was shown in Ref. [22]. The method and applications of the MCSM were reviewed, for instance, in Refs. [20, 23]. The MCSM is the methodology fully exploited in this work. It uses Slater determinants as the basis vectors, similarly to the conventional shell-model calculation. However, the Slater determinants are not the same as those used in the conventional shell-model calculation. In the conventional one, each Slater determinant is a direct product of some single-particle states, each of which is a magnetic substate of the single-particle orbital.

An MCSM eigenstate is schematically written as (see Ref. [52] for more detailed but pedagogical concise explanation),

$$\Psi = \sum_k f_k \hat{P}_{J^P} \phi_k, \quad (\text{B1})$$

where f_k denotes the amplitude, \hat{P}_{J^P} means the projection operator on to the spin/parity J^P (this part is more complicated in practice), and ϕ_k stands for Slater determinant called (k -th) MCSM basis vector: $\phi_k = \Pi_i c_i^{(k)\dagger} |0\rangle$. Here, $|0\rangle$ is the inert core (closed shell), $c_i^{(k)\dagger}$ refers to a superposition,

$$c_i^{(k)\dagger} = \sum_n D_{i,n}^{(k)} a_n^\dagger, \quad (\text{B2})$$

with a_n^\dagger being the creation operator of a usual single-particle state, for instance, that of the HO potential, and $D_{i,n}^{(k)}$ denoting a matrix element. By choosing an optimal matrix $D^{(k)}$, we can select ϕ_k so that such ϕ_k better contributes to the lowering of the corresponding energy eigenvalue. Thus, the determination of $D^{(k)}$ is the core of the MCSM calculation. The index k runs up to 50-100, but can be more. These are much smaller than the dimension of the many-body Hilbert space, which is 4.8×10^{33} for the case of ^{166}Er , as already mentioned.

Thus, the basis vectors of the MCSM calculation are composed of “stochastically - variationally deformed” single-particle states. The adopted basis vectors are mutually independent, otherwise no energy gain. By having a set of these MCSM basis vectors thus fixed, we diagonalize the Hamiltonian, and obtain energy eigenvalues and eigenstates. A large number of MCSM calculations have been performed as exemplified in Refs. [24–34, 40, 70].

Besides the breakthrough in the computational limit, the MCSM also has the advantage of providing a very useful way to visualize the intrinsic shape of each MCSM eigenstate through what is called the T-plot [40, 70]. Because the MCSM basis vector is a deformed Slater determinant, one can calculate its intrinsic quadrupole moments, *i.e.* the quadrupole moments in the body-fixed frame, denoted as Q_0 and Q_2 . They can be expressed by two parameters β_2 and γ , as described in the main text. The importance of each MCSM basis vector to a given eigenstate (its overlap probability in the MCSM eigenstate) is represented by the size (area) of its circular symbol in the T-plot. The T-plot can be made on the β_2 - γ plane, but is usually on the PES, and intuitively exhibits the underlying physical pictures for the states of interest, as demonstrated in a variety of studies, *e.g.* in Refs. [24–28, 30, 31, 34].

We stress that the T-plot played a major role in the present study, displaying not only triaxial shapes of the eigenstates but also their rigidity over different eigenstates.

The present calculation was performed by the most advanced methodology of the MCSM. This is called Quasiparticle Vacua Shell Model (QVSM) [35]. In the original version of the MCSM, the pairing correlations are mainly incorporated by superposing different MCSM basis vectors, which are deformed Slater determinants as stated above. The QVSM basis vectors are somewhat like a Hartree-Fock-Bogoliubov ground state (which is a generalization of the BCS ground state), and this feature enables each QVSM basis vector to contain both effects of the deformed mean field and effects of the pairing correlations. This advantage is particularly exploitable for heavy nuclei where the pairing correlations over different single-particle orbitals become more important than for lighter nuclei. In the original MCSM, the pairing correlations are largely carried by superpositions of different MCSM basis vectors. As the QVSM calculation is computationally heavier, this merit makes sense for some nuclei heavier than $A \sim 100$.

The spurious center-of-mass motion is removed to a sufficient extent by the Lawson method [71].

REFERENCES

1. Bohr, A. & Mottelson, B.R., Nuclear Structure (Benjamin, New York, 1975), Vol. II.
2. Bohr, A., The Coupling of Nuclear Surface Oscillations to the Motion of Individual Nucleons, *Mat. Fys. Medd. Dan. Vid. Selsk.* **26**, 14 (1952).
3. Rainwater, J., Nuclear energy level argument for a spheroidal nuclear model, *Phys. Rev.* **79**, 432 (1950).
4. Bohr, A. Rotational Motion in Nuclei. In *Nobel Lectures, Physics 1971–1980*, Lundqvist S., Ed.;

- World Scientific: Singapore, 1992; pp. 213–232; <https://www.nobelprize.org/prizes/physics/1975/bohr/facts/>.
5. Atkins, P., de Paula, J., Keeler J., Physical Chemistry (Oxford University Press, Oxford, 2018).
 6. National Nuclear Data Center. NuDat 3.0. <https://www.nndc.bnl.gov/nudat3/>
 7. Jahn, H. A., Teller, E., Stability of Polyatomic Molecules in Degenerate Electronic States I - Orbital Degeneracy, *Proc. R. Soc. A*, **161**, 220, (1937).
 8. Rowe, D. J., Nuclear collective motion:: models and theory, (World Scientific, Singapore, 2010).
 9. De Shalit, A., Feshbach, H., Nuclear Structure (theoretical Nuclear Physics), (John Wiley and Sons, New York, 1974).
 10. Ring, P., Schuck, P., The Nuclear Many-Body Problem, (Springer-Verlag: Berlin, 1980).
 11. Nix, J. R., Further studies in the liquid-drop theory of nuclear fission, *Nucl. Phys. A* **130**, 241 (1969).
 12. Ichikawa, T., Iwamoto, A., Möller, P., Sierk, A. J., Contrasting fission potential-energy structure of actinides and mercury isotopes, *Phys. Rev. C* **86**, 024610 (2012).
 13. Kumar, K., & Baranger, M., Nuclear deformations in the pairing-plus-quadrupole model (III). Static nuclear shapes in the rare-earth region, *Nucl. Phys. A* **110**, 529 (1968). *Proc. R. Soc. A*, **161** 220, (1937).
 14. Bes, D.R., & Sorensen, R.A., The Pairing-Plus-Quadrupole Model. *Advances in Nuclear Physics*, Eds: Baranger, M. & Vogt, E., (Plenum Press, New York, 1969), vol. ??, (Benjamin, New York, 1975), Vol. II.
 15. Elliott, J.P., Collective motion in the nuclear shell model I. Classification schemes for states of mixed configurations, *Proc. Roy. Soc. (London) A* **245**, 128 (1958).
 16. Elliott, J.P., Collective motion in the nuclear shell model II. The introduction of intrinsic wave-functions, *Proc. Roy. Soc. (London) A* **245**, 562 (1958).
 17. Caurier, E., Martínez-Pinedo, G., Nowacki, F., Poves, A., Zuker, A. P., The shell model as a unified view of nuclear structure, *Rev. Mod. Phys.* **77**, 427 (2005)
 18. National Nuclear Data Center. Evaluated Nuclear Structure Data File. <http://www.nndc.bnl.gov/ensdf/>.
 19. Bohr, A. & Mottelson, B.R. Nuclear Structure (Benjamin, New York, 1969), Vol. I.
 20. Otsuka, T., Honma, M., Mizusaki, T., Shimizu, N. & Utsuno, Y., Monte Carlo Shell Model for Atomic Nuclei, *Prog. Part. Nucl. Phys.* **47**, 319-400 (2001).
 21. Honma, M., Mizusaki, T., Otsuka, T., Diagonalization of Hamiltonians for Many-Body Systems by Auxiliary Field Quantum Monte Carlo Technique, *Phys. Rev. Lett.* **75**, 1284 (1995).
 22. Otsuka, T., Mizusaki, T., Honma, M., Structure of the N=Z=28 Closed Shell Studied by Monte Carlo Shell Model Calculation, *Phys. Rev. Lett.* **81**, 1588 (1998).
 23. Shimizu, N. *et al.*, New-generation Monte Carlo shell model for the K computer era, *Prog. Theor. Exp. Phys.* **2012**, 01A205 (2012).
 24. Togashi, T., Tsunoda, Y., Otsuka, T., & Shimizu, N., Quantum Phase Transition in the Shape of Zr isotopes, *Phys. Rev. Lett.* **117**, 172502 (2016).
 25. Leoni, S., *et al.*, Multifaceted Quadruplet of Low-Lying Spin-Zero States in ^{66}Ni : Emergence of Shape Isomerism in Light Nuclei, *Phys. Rev. Lett.* **118**, 162502 (2017).
 26. Togashi, T., Tsunoda, Y., Otsuka, T., Shimizu, N., & Honma, M., Novel Shape Evolution in Sn Isotopes from Magic Numbers 50 to 82, *Phys. Rev. Lett.* **121**, 062501 (2018).
 27. Marsh, B. A. *et al.* Characterization of the shape-staggering effect in mercury nuclei, *Nature Physics* **14**, 1163-1167 (2018).
 28. Ichikawa, Y. *et al.*, Interplay between nuclear shell evolution and shape deformation revealed by the magnetic moment of ^{75}Cu , *Nature Physics* **15**, 321 (2019).
 29. Taniuchi, R. *et al.*, ^{78}Ni revealed as a doubly magic stronghold against nuclear deformation, *Nature* **569**, 53 (2019).
 30. Otsuka, T., Tsunoda, Y., Abe, T., Shimizu, N., Van Duppen, P., Underlying Structure of Collective Bands and Self-Organization in Quantum Systems, *Phys. Rev. Lett.* **123**, 222502 (2019).
 31. Märginean, S., *et al.*, Shape Coexistence at Zero Spin in ^{64}Ni Driven by the Monopole Tensor Interaction, *Phys. Rev. Lett.* **125**, 102502 (2020)
 32. Tsunoda, N., Otsuka, T., Takayanagi, K., Shimizu, N., Suzuki, T., Utsuno, Y., Yoshida, S., & Ueno, H., The impact of nuclear shape on the emergence of the neutron dripline, *Nature* **587**, 66 (2020).
 33. Abe, T., Maris, P., Otsuka, T., Shimizu, N., Utsuno, Y., Vary, J. P., Ground-state properties of light $4n$ self-conjugate nuclei in ab initio no-core Monte Carlo shell model calculations with nonlocal NN interactions, *Phys. Rev. C* **104**, 054315 (2021).
 34. Otsuka, T., Abe, T., Yoshida, T., Tsunoda, Y., Shimizu, N., Itagaki, N., Utsuno, Y., Vary, J., Maris, P., Ueno, H., α -Clustering in atomic nuclei from first principles with statistical learning and the Hoyle state character, *Nature Communications* **13**, 2234 (2022).
 35. Shimizu, N., Tsunoda, Y., Utsuno, Y., Otsuka, T., Variational approach with the superposition of the symmetry-restored quasiparticle vacua for nuclear shell-model calculations, *Phys. Rev. C* **103**, 014312 (2021).
 36. Otsuka, T., Suzuki, T., Honma, M., Utsuno, Y., Tsunoda, N., Tsukiyama, K., and Hjorth-Jensen, M., Novel features of nuclear forces and shell evolution in exotic nuclei, *Phys. Rev. Lett.* **104**, 012501 (2010).
 37. Brown, B. A., Double-Octupole States in ^{208}Pb , *Phys. Rev. Lett.* **85**, 5300 (2000).
 38. Utsuno, Y., Shimizu, N., Otsuka, T., Yoshida, T., Tsunoda, Y., Nature of Isomerism in Exotic Sulfur Isotopes. *Phys. Rev. Lett.*, **114**, 032501 (2015).
 39. Otsuka, T., Shimizu, N., Tsunoda, Y., Moments and radii of exotic Na and Mg isotopes. *Phys. Rev. C* **105**, 014319 (2022).
 40. Tsunoda, Y., Otsuka, T., Shimizu, N., Honma, M., Utsuno, Y., Novel shape evolution in exotic Ni isotopes and configuration-dependent shell structure, *Phys. Rev. C* **89**, 031301(R) (2014).
 41. Samorajczyk-Pysk, J., *et al.*, Low-spin levels in ^{140}Sm : Five 0^+ states and the question of softness against nonaxial deformation, *Phys. Rev. C*, **104**, 024322 (2021).
 42. Tsunoda, Y., Otsuka, T., Triaxial rigidity of ^{166}Er and its Bohr-model realization, *Phys. Rev. C*, **103**, L021303 (2021).
 43. Here, the proton-neutron interaction actually means the multipole part of it. Any given interaction can be decomposed into the monopole part and the multipole part, of which the former will be discussed in Sec. VI. The multipole part is the rest of the interaction, and can be the direct source to produce the surface deformation of atomic nuclei, if it occurs in their ground or low-lying states.
 44. Sharpey-Schafer, J. F., Bark, R. A., Bvumbi, S. P., Dinoko, T. R. S., and Majola, S. N. T., “Stiff” deformed nuclei, configuration dependent pairing and the β and γ degrees of freedom, *Eur. Phys. J. A*, **55**, 15 (2019).
 45. Sun, Y., Hara, K., Sheikh, J. A., Hirsch, J. G., Velázquez, V., Guidry, M., Multiphonon γ -vibrational bands and the triaxial projected shell model. *Phys. Rev. C* **61**, 064323 (2000).
 46. Fahlander, C., Axelsson, A., Heinebrodt, M., Hartlein, T., Schwalm, D., Two-phonon γ -vibrational states in ^{166}Er , *Phys.*

- Lett. B **388**, 475 (1996).
47. Garrett, P. E.; Kadi, M.; Li, Min; McGrath, C. A.; Sorokin, V.; Yeh, Minfang; Yates, S. W., $K^\pi=0^+$ and 4^+ Two-Phonon γ -Vibrational States in ^{166}Er , Phys. Rev. Lett. **78**, 4545 (1997).
 48. Davydov, A.S., Filippov, G.F., Rotational states in even atomic nuclei, Nucl. Phys. **8**, 237 (1958).
 49. Davydov, A.S., Rostovsky, V.S., Relative transition probabilities between rotational levels of non-axial nuclei. Nucl. Phys. **12**, 58 (1959).
 50. Boutachkov, P., Aprahamian, A., Sun, Y., Sheikh, J.A., Frauendorf, S., In-band and inter-band B(E2) values within the Triaxial Projected Shell Model. Eur. Phys. J. A **15**, 455 (2002).
 51. Otsuka, T., Gade, A., Sorlin, O., Suzuki, T., Utsuno, Y. Evolution of shell structure in exotic nuclei, Rev. Mod. Phys. **92**, 015002 (2020).
 52. Otsuka, T., Emerging concepts in nuclear structure based on the shell model, Physics **4**, 258 (2022), <https://www.mdpi.com/2624-8174/4/1/18>.
 53. Otsuka, T., Suzuki, T., Fujimoto, R., Grawe, H., Akaishi, Y., Evolution of the nuclear shells due to the tensor force, Phys. Rev. Lett. **95**, 232502 (2005).
 54. Yukawa, H., On the Interaction of Elementary Particles. I, Proc. Phys. Math. Soc. Japan **17**, 48 (1935)
 55. Bethe, H. A., The Meson Theory of Nuclear Forces I. General Theory, Phys. Rev. **57**, 260 (1940)
 56. Osterfeld, F., Nuclear spin and isospin excitations, Rev. Mod. Phys. **64**, 491 (1992)
 57. Tsunoda, N., Otsuka, T., Tsukiyama, K., Hjorth-Jensen, M., Renormalization persistency of the tensor force in nuclei, Phys. Rev. C **84**, 044322 (2011).
 58. Tajima, N., Takahara, S., Onishi, N., Extensive Hartree-Fock+BCS calculation with Skyrme SIII force, Nucl. Phys. A **603** 23 (1996).
 59. Möller, P., Bengtsson, R., Carlsson, G., Olivius, P., Ichikawa, T., Global Calculations of Ground-State Axial Shape Asymmetry of Nuclei, Phys. Rev. Lett. **97**, 162502 (2006).
 60. Hayashi, A., Hara, K., Ring, P., Existence of Triaxial Shapes in Transitional Nuclei. Phys. Rev. Lett. **53**, 337 (1984).
 61. Weinberg, S., Nuclear forces from chiral lagrangians, Phys. Lett. B **251**, 288 (1990).
 62. Machleidt, R., Entem, D. R., Chiral effective field theory and nuclear forces, Phys. Rep. **503**, 1 (2011).
 63. Pietralla, N., von Brentano, P., Herzberg, R.-D., Kneissl, U., Lo Iudice, N., Maser, H., Pitz, H. H., Zilges, A., Systematics of the excitation energy of the 1^+ scissors mode and its empirical dependence on the nuclear deformation parameter, Phys. Rev. C **58**, 184 (1998).
 64. Giacalone, G., A matter of shape: seeing the deformation of atomic nuclei at high-energy colliders, Ph.D thesis, Université Paris-Saclay, CNRS, CEA, <https://arxiv.org/abs/2101.00168>.
 65. Frauendorf, S., Spontaneous symmetry breaking in rotating nuclei, Rev. Mod. Phys. **73**, 463 (2001)
 66. Benrabia, K., Medjadi, D. E., Imadalou, M., Quentin, P., Triaxial quadrupole dynamics and the inner fission barrier of some heavy even-even nuclei, Phys. Rev. C **96**, 034320 (2017).
 67. Larsson, S. E., Leander, G., Fission Barriers for Heavy Elements with Quadrupole, Hexadecapole and Axially Asymmetric Distortions Taken into Account Simultaneously, *Physics and Chemistry of Fission 1973, Proc. of the 3rd IAEA Symposium on the Physics and Chemistry of Fission* (International Atomic Energy Agency, Vienna, 1974), vol. I, p. 177.
 68. Talmi, I., Simple Models of Complex Nuclei: The Shell Model and Interacting Boson Model, (CRC Press, Boca Raton, 2017).
 69. Shimizu, N., Mizusaki, T., Utsuno, Y. & Tsunoda, Y., Thick-Restart Block Lanczos Method for Large-Scale Shell-Model Calculations, Comp. Phys. Comm. **244**, 372 (2019).
 70. Otsuka, T. and Tsunoda, Y., The role of shell evolution in shape coexistence, J. Phys. G, **43**, 024009 (2016).
 71. Gloeckner, D. H. and Lawson, R. D., Spurious Center-of-Mass Motion, Phys. Lett. B **53**, 313 (1974).